Spectrochimica Acta Part A: Molecular and Biomolecular Spectroscopy 278 (2022) 121322

Contents lists available at ScienceDirect

Spectrochimica Acta Part A: Molecular and Biomolecular Spectroscopy

journal homepage: www.elsevier.com/locate/saa

New physical insights: Formamide discharge decomposition and the role of fragments in the formation of large biomolecules

Adam Pastorek [a,b], Victoria H.J. Clark [c], Sergei N. Yurchenko [c], Martin Ferus [a], Svatopluk Civiš [a,*]

[a] J. Heyrovsky Institute of Physical Chemistry, Czech Academy of Sciences, Dolejškova 2155/3, 18200 Prague 8, Czech Republic
[b] Faculty of Nuclear Sciences and Physical Engineering, Czech Technical University in Prague, Břehová 78/7, 11519 Prague 1, Czech Republic
[c] Faculty of Mathematics and Physical Sciences, University College London, Gower Street, London WC1E 6BT, United Kingdom

HIGHLIGHTS

- T-R FTIR spectroscopy of CO, CN, N_2, HCN and CO_2.
- Generation of species in glow discharge of formamide-N_2-H_2O-He mixture.
- Analysis of decomposition products together with time profiles.
- Energy transfer between excited nitrogen and CO.
- Non-LTE modelling of obtained spectra for individual species.

GRAPHICAL ABSTRACT

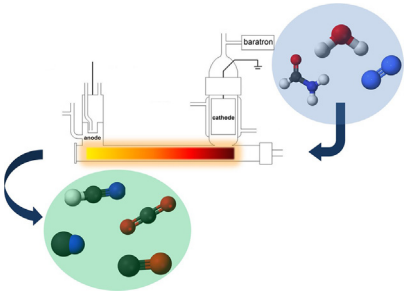

ARTICLE INFO

Article history:
Received 6 October 2021
Received in revised form 21 April 2022
Accepted 25 April 2022
Available online 30 April 2022

ABSTRACT

In this work we present a time-resolved FTIR spectroscopic study on kinetics of atomic and molecular species, specifically CO, CN radical, N_2, HCN and CO_2 generated in a glow discharge of formamide-nitrogen-water mixture in a helium buffer gas. Radicals such as NH, CH and OH have been proven to be fundamental stones of subsequent chemical reactions having a crucial role in a prebiotic synthesis of large organic molecules.

This work contains three main goals. Firstly, we present our time-resolved spectra of formamide decomposition products and discuss the mechanism of collisional excitations between specific species. Secondly, according to our time resolution, we demonstrate and explain the band shape of CO's first overtone and the energy transfer between excited nitrogen and CO, present in our spectra. Lastly, we present theoretical results for the non-LTE modelling of the spectra using bi-temperature approach and a 1D harmonic Franck-Condon approach for the multi-molecule spectra of the formamide decomposition process in the 1800–5600 cm^{-1} spectral range.

1. Theoretical background

Since Oparin's work on abiogenesis [1], there have been many attempts to simulate such reactions in the laboratory environment. Starting with famous Miller-Urey experiment [2], researchers tried many combinations of initial mixtures, like hydrogen cyanide, urea, acetonitrile, formaldehyde, formic acid, glycol aldehyde and others; when applying different energy sources, e. g. electric discharge [3,4], asteroid impact simulation by laser spark [5–7], UV radiation [8], proton radiation [9,10], gamma radiation [11] or simple heating [12–15].

Among all initial mixtures used for the aforementioned combination experiments, two parent compounds stood out during past 10 years – hydrogen cyanide [16–22] and formamide [23–28] (which is a hydration product of HCN). This work is focused on products of the formamide decomposition inside of the helium positive column glow discharge.

* Corresponding author.
E-mail address: svatopluk.civis@jh-inst.cas.cz (S. Civiš).

https://doi.org/10.1016/j.saa.2022.121322
1386-1425/

Formamide structure ($HCONH_2$) contains four biogenic elements (C, N, O, H) and serves as a simplest possible representation of a peptide linkage. The presence of formamide has been proven in interstellar space, on young stars [29,30] and comets [31,32]. By use of the sources of external energy mentioned above, formamide decomposes and reacts with hydrogen cyanide or short-lived radicals such as CN, NH_2 or H. In subsequent reaction chains, nucleobases, sugars, amino acids, fatty acids and other prebiotic compounds can be formed.

Hydrolysis of HCN [33], presumed to be dissolved in early Earth's seawater [34], could potentially serve as another source of formamide. Together with volcanic activity [35] and plasma reprocessing of atmospheric mixtures [36–38], hydrolysis can be considered as endogenous source of formamide. It is important to note that formamide is sufficiently stable and therefore has a strong potential for accumulation over time [39].

Whether formamide was one of the most important compounds during the first steps of large organic synthesis or not, our previous experiments show that most of the mechanisms of prebiotic reactions (application of external energy onto simple compounds and mixtures) is mainly mediated by the radicals. In the past, we monitored the decomposition products of formamide in a pulsed glow discharge, containing CN radical and molecules like CO, CO_2, HNC and HCN in the presence of atomic fragments (H, N, C and O), to study the HNC/HCN ratio, where this ratio was found to be around 2.2–3%. This study confirmed the dominant role of radicals, during the formation of HCN and HNC. The key role of CN radical was proven during spectroscopic studies on high energy laser sparks generated in formamide [40,41], where CN radical plays a dominant role when forming large molecules like diaminomaleonitrile via 2-amino-2-hydroxyacetonitrile and 2-amino-2-hydroxymaleonitrile.

The radical chemistry was also studied in different chemical mixtures exposed to the glow discharge. For example, methane mixture with helium buffer gas [42] produces CH radical together with large stable organic products (e.g. acetylene). In another study, the oxidizing effect of OH radical onto CO molecule inside of high energy laser spark was investigated [43].

Molecules and radicals such as CO, CN, NH, OH and CH are very rigid species, mostly with double or triple bond between the atoms. They can absorb large energy amounts which is then distributed in many highly excited energy levels of various vibronic states [44,45] without any splitting of the molecular bond. Due to this fact, CN radicals can act as an energy mediator via collisional interactions and the absorbed energy is easily transferred to other species and creates common bonding complexes. CN radical is a discharge product which can be found in the discharge or laser spark of almost all molecules containing nitrogen and carbon atoms [16].

Apart from collisional effects, the dissociation of large molecules into smaller fragments can lead to a non-equilibrium population of the fragments' internal energy levels [17]. The vibrational and rotational degrees of freedom within a molecule, which are usually populated in accordance with the Boltzmann distribution, can be populated to a higher level than would ordinarily be expected for the thermal conditions [46]. Assuming that dissociation happens instantly, the fragments (diatomics or triatomics) are formed with structural properties of the pre-dissociation system (bond lengths and angles), which are very different from the corresponding gas phase molecules. These structural differences between the fragment and gas phase molecules, and associated internal stress, result in non-Boltzmann vibrational and rotational excitations, which carry the memory of the original system. Depending on the environment, the rotational populations usually equilibrate very quickly, while the non-local thermal equilibrium (non-LTE) vibrational excitations can live long enough to be detected and spectroscopically analysed. Molecules with non-LTE are unique spectroscopic signatures owing to the excess population of vibrational molecules within their spectra, and analysis of said spectra can yield important information of the dissociation pathway taken by the resultant fragments [47].

The modelling of non-LTE molecules is not trivial and there is no singular method for doing so. Dedicated programs exist for the modelling of some non-LTE effects, for example within interstellar line spectra [48], radiative transfer [49–51], stellar atmospheres [52,53], and accretion disks [54].

In addition to the dedicated programs, non-LTE calculations have been performed for a range of atomic and molecular problems including, for example, the emission modelling in plasmas [55], exoplanet atmospheres, atomic abundancies [56–58], molecular abundancies [59], galactic chemical evolution [60], inelastic collisions [61,62], and dissociative reaction path determinations [47].

In this study, we present a time-resolved study of the nitrogen-water-formamide discharge in helium buffer gas. The use of time-resolved Fourier transform spectroscopy (FT) opens new pathways and new points of view in study of the formation and decomposition processes inside the discharge plasma and permits description of the dynamics of the formation and decay of excited states of presented molecules. Here, we are able to study the individual processes using atomic or molecular lines in a wide spectral range of the FT technology, which is extended into the time dimension. The FT technique was used to investigate the time profiles of the emission spectra before, during and after the discharge pulse. We discovered new many-molecule non-LTE model for the spectrum several μs after the discharge pulse is presented.

We also calculate the non-LTE spectra of the fragments assuming a bi-temperature approach based on the Treanor distribution [63] and a 1D harmonic Franck-Condon approach. The rotational states are assumed to be populated according with the Boltzmann distribution for some rotational temperature T_R. The vibrational states are either populated by the Boltzmann distribution or assumed to be produced through an effective dissociative pathway, with excitations estimated via a Franck-Condon approximation.

The 1D harmonic approach used is based on our previous work [64], and use the variety of techniques to achieve the best non-LTE fit with experiment.

2. Experimental arrangement

The emission spectra from a positive column of formamide-water-nitrogen discharge plasma mixtures were observed with the time-resolved Fourier transform high-resolution Bruker IFS 120 HR interferometer. The discharge tube, covered with an outer glass jacket, was 25 cm long with an inner diameter equal to 12 mm. The AC discharge was maintained by a high voltage transistor switch HTS 81 (Behlke electronic GmbH, Frankfurt, Germany) applied between the stainless steel anode and the grounded cathode. The discharge plasma was cooled by running water in the outer jacket of the cell. The voltage drop across the discharge was 1.4 kV, with a pulse width of 22 μs and 0.5 A peak-to-peak current. The scanner velocity of FTS was set to produce a 10 kHz He–Ne laser fringe frequency, which was used to trigger the discharge pulse. The recorded spectral range was 1800–5600 cm^{-1} with an optical filter, at an unapodized resolution of 0.05 cm^{-1}, by use of InSb liquid nitrogen cooled detector. 50 scans were averaged to obtain a reasonable signal-to-noise ratio. The initial pressure of He was changed from 2 to 10.8 Torr and enriched by vapours of formamide (FA) mixed with nitrogen and water (total partial pressure of 0.2 Torr and 1:1:1 ratio). The experimental setup is depicted in Fig. 1.

The continuous scanning principle was the basis for data acquisition by a modified (Bruker IFS 120) spectrometer in our labora-

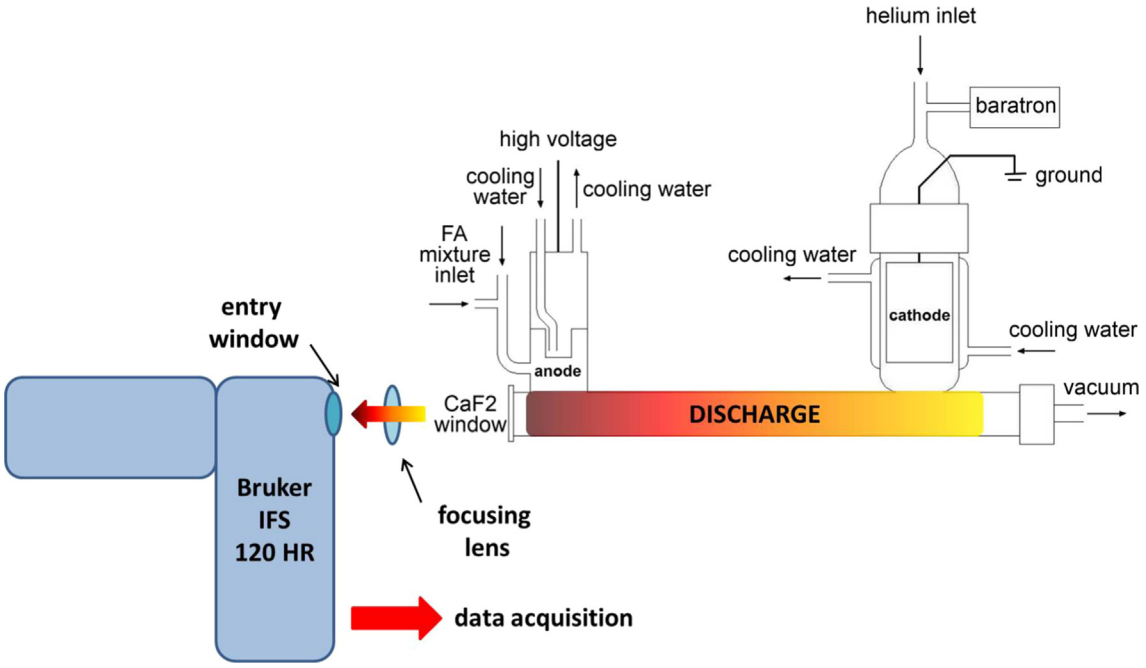

Fig. 1. The experimental setup.

tory at the J. Heyrovsky Institute of Physical Chemistry (Fig. 2). The data acquisition system can be described as follows: the position of the traversing mirror of the Michelson interferometer is detected by reading the interference maxima (fringes) of the HeNe laser emission. The input signal in a cosine function shape is digitally processed into rectangular pulses and becomes the internal standard of the interferometer. The frequency of these rectangular pulses depends on the mirror speed. In the classic measurement mode, the frequency is usually 10 kHz with a pulse duration of 100 μs. An external processor monitors the beginning of the HeNe laser digital pulse, its order and the zero position of the mirror. During one pulse, the signal from the detector is read (30–64 readings), this is the so-called AD trigger [65,66]. A discharge pulse of variable length can be arbitrarily inserted into the data acquisition process (AD trigger). This process results in 30 to 64 reciprocally time-shifted interferograms (spectra).

Here in the presented paper, we used 30 data acquisition points (AD trigger) in a 3-microsecond time interval, which covers the 90-μs time scale. The pulse width was 22 μs.

3. Non-LTE modelling

We present a variety of empirical non-local thermodynamic equilibrium (non-LTE) models to describe the intensity pattern of

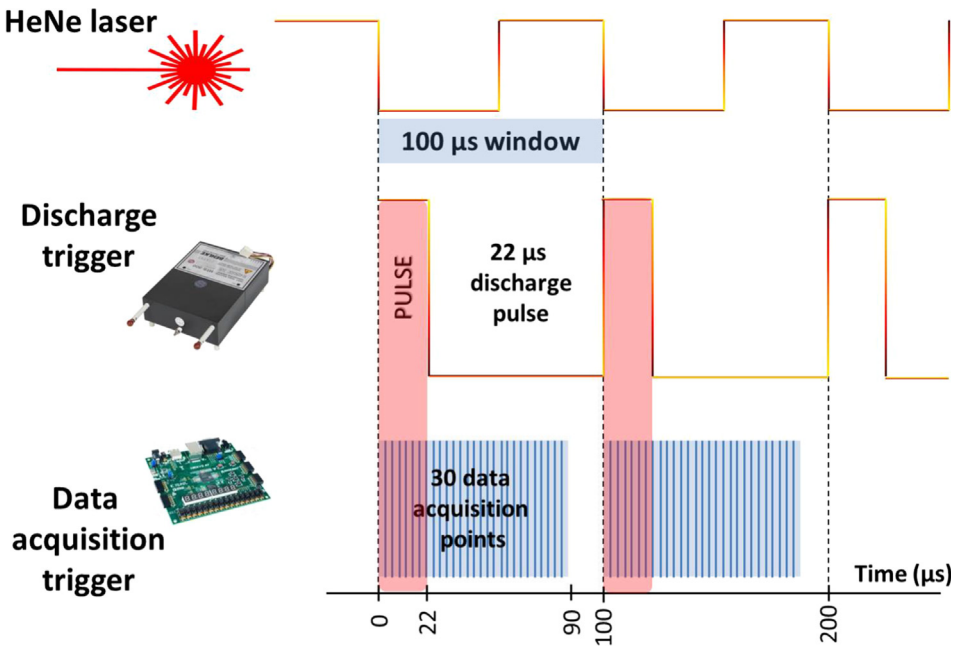

Fig. 2. The time-resolved data acquisition setup.

the formamide discharge experimental spectrum between 1800 cm^{-1} and 5600 cm^{-1} by simulating the corresponding non-LTE vibrational spectra of N_2, CO, CN, HCN and CO_2, the five molecules determined to be present via experimental procedure. In this section, the details and methodologies of all approaches shall be described in detail.

3.1. Bi-temperature

The bi-temperature approach uses the Treanor distribution [63] for energy level population, with rotational and vibrational states described by the corresponding LTE distributions. The separate temperatures for rotations and vibrations are used to calculate the respective energies, and the total energy is approximated as the sum of the rotational and vibrational energies.

$$\tilde{E}_{J,v,k} = \tilde{E}_v^{vib} + \left(\tilde{E}_{J,v,k} - \tilde{E}_v^{vib}\right) \tag{1}$$

where v and k are the vibrational and rotational quantum numbers, respectively and $\left(\tilde{E}_{J,v,k} - \tilde{E}_v^{vib}\right)$ is the rotational energy contribution.

The non-LTE distribution of the spectrum then arises from the product of the vibrational and rotational distributions [67,68].

$$F_{J,v,k}(T_v, T_R) = g_{J,v,k}\frac{e^{-c_2\tilde{E}_v^{vib}/T_V}e^{-c_2\tilde{E}_{J,k}^{v,rot}/T_R}}{Q(T)} \tag{2}$$

where $c_2 = hc/k_B$ is the second radiation constant, $\tilde{E}_i = E_i/hc$ is the energy term value, $g_{J,v,k}$ is the state degeneracy and T_V and T_R are the vibration and rotation temperatures, respectively. In Eq. (2), $Q(T)$ is the non-LTE partition function defined as

$$Q(T) = \sum\nolimits_n g_n^{ns}(2J_n + 1)F_{J,v,k}(T_V, T_R) \tag{3}$$

where g_n^{ns} is is the nuclear-spin statistical weight factor and J_n is the corresponding total angular momentum.

Emission line intensity I_{if} (in photon/s per molecule per steradian) for a transition $i \to f$ with the wavenumber $\tilde{\nu}_{if}$ is then given by

$$I(i \to f) = F_{J',v',k'}A(i \to f) \tag{4}$$

where A_{if} is the Einstein-A coefficient and $F_{J',v',k'}$ is the population of the upper state.

3.2. 1D harmonic Franck-Condon approach

This 1D method adapts the original LTE ExoMol line lists for the required molecule and incorporates the non-LTE effects of the fragmentation. This methodology has been described extensively elsewhere [47] and in this publication we shall only describe details pertinent to these calculations. We have shown in previous publications that this method can accurately calculate the non-LTE spectra for small molecules [47,64]. In this work we show that the 1D harmonic wavefunction methodology can be used as an alternative to the bi-temperature one to model non-LTE populations of molecules.

The basis for this methodology is a harmonic approximation assuming a Franck-Condon-like model such as was described by Band and Freed [69] where all degrees of freedom were completely separable. This method of using the structural differences between reactant and product was previously used by Berry in 1974 [70]. The naming convention used in the following section is "Gas phase" = equilibrium gas phase, LTE molecule; "Fragment" = non-LTE molecule fragmented from formamide. In this paper we use the 1D harmonic Franck-Condon approach as an effective 1D model which considers "Fragment" as some reference diatomic system with the structure adjusted to reproduce the experimental population as follows.

The vibrational populations of the fragments are estimated from the Franck-Condon factors $\langle v'' = 0(\text{fragment})|v'(\text{gasphase})\rangle$ i.e. overlap integrals between the "fragment" wavefunction $|v''\rangle$ (which is assumed to be in its ground vibrational state) and the "gas phase" wavefunctions $|v'\rangle (v' = 0 \le x \le 30)$:

$$N_v^{vib} = \langle 0(\text{fragment})|v(\text{g.ph.})\rangle^2 \tag{5}$$

where N_v^{vib} are the population densities for each vibrational energy level of the gas phase (g.ph.) molecule (see Clark & Yurchenko [47] for details).

Both vibrational wavefunctions $|v\rangle$ of the "fragment" and "gas-phase" molecule are approximated by 1D Harmonic oscillators:

$$\Psi_v = C_v H_v(x)e^{\frac{-x^2}{2}} \tag{6}$$

where

$$x = \frac{r - r_e}{\sqrt{\alpha}}, \tag{7}$$

$$\alpha = \sqrt{\frac{h}{4\pi^2 c\mu\omega_e}}, \tag{8}$$

μ is the reduced mass, which for a diatomic is given by:

$$\frac{1}{\mu} = \frac{1}{m_x} + \frac{1}{m_y}, \tag{9}$$

h is the Planck constant, c is the speed of light, m_x is the nuclear mass of an atom x, in Da, and m_y is the nuclear mass of an atom y, in Da.

We use corresponding empirical values r_e and ω_e for the equilibrium parameter and harmonic frequency constant of the "gas-phase" partner. The corresponding equilibrium parameters of the "fragment" are treated as adjustable parameters determined by adjusting the shape of bands of the fragment molecules until the best fit with experiment was achieved. In principle, these best fit values could be associated with a dissociation pathway. [40,71–75] However due to other processes involved such as collisions with other molecules as well as with electrons, the information about the dissociation pathway of formamide can be partly "overwritten" by other relaxation processes. In this case the parameters r_e and ω_e should be treated as effective values, with no immediate physical interpretation, but as part of our non-LTE representation.

The calculated populations N_v^{vib} were then combined with the ExoMol line list to give a weighting for all transitions in the ExoMol line list in question. This is done by incorporating the non-LTE vibrational densities into the ExoMol States file (the ExoMol file formats are discussed extensively elsewhere) [76]. The non-LTE spectrum of the molecule [77–85] for a given T and P are then calculated using the Einstein-A coefficients for the molecule as provided by ExoMol (https://www.exomol.com) with the ExoCross program [67].

The rotational populations are assumed to be in LTE. The final ro-vibrational population is thus given by

$$N_{rv} = \frac{N_v^{vib}(2J + 1)}{Q}e^{\frac{-c_2\tilde{E}_J^{rot}}{T_R}}. \tag{10}$$

Here c_2 is the second radiation constant and $\tilde{E}_J^{rot}$ is the rotation contribution to $\tilde{E}_{J,v}$ (rovibrational energy term value) for a given vibrational state defined as

$$\tilde{E}_J^{rot} = \tilde{E}_{J,v} - \tilde{E}_v^{vib}, \quad (11)$$

and Q is the partition function. Here we apply our 1D model as an alternative to the bi-temperature model to simulate the molecule non-LTE features of the discharged formamide shown in Fig. 3.

In this study we did not go beyond this simplistic one-dimensional Harmonic model (see e.g. Clark & Yurchenko [47]). This model was sufficient for the purposes of modelling of the bi-temperature non-LTE vibrational populations observed. We also did not see strong influence from the dissociation pathways where multidimensional Franck-Condon integrals might become important [47].

4. Results and discussion

4.1. Time resolved high resolution FT emission spectroscopy

The method of time resolved spectroscopy was chosen for the detection of unstable species produced by formamide dissociation in plasma in a spectral range of 1800–5600 cm^{-1}. This method allows obtaining time patterns of emission intensities of unstable species and its sensitivity of detection of those substances is higher than in the case of non-time-resolved one. In the emission spectrum, depicted in Fig. 3, we detected atomic lines of He I (e.g. strong lines ^3D-$^3F^0$ around 2476.6 cm^{-1}, line ^1S-$^1P^0$ at 4857.45 cm^{-1} and lines ^3D-$^3F^0$ around 5350.3 cm^{-1}), together with dominant, very strong emission bands of series of electronic rotational-vibrational transitions of the excited CN radical: $A^2\Pi - X^2\Sigma^+, \Delta v = -2, -3$; then the electronic transitions of N_2 and a series of very strong highly excited rotational-vibrational transitions of carbon monoxide, carbon dioxide and hydrogen cyanide.

4.2. Time profiles

Our time resolved infrared spectroscopy gives the possibility for creation time profiles of the individual species from the set of time shifted spectra. The time-resolved emission profiles of the H, N, C and O atomic emission (panel A), CO emission (panel B), N_2 emission (panel C) and CN electronic transition (panel D) are compared in Fig. 4.

Panel A of Fig. 4 shows the production and decay profile based on atomic emission line intensities in our discharge spectra. All atoms have the same behaviour, with the maximum intensity around 3 μs after the discharge pulse, which quickly decreases in a time period of 15 μs. After 40 μs, the intensity of atoms fluctuates around the noise level. Atoms like H, N, C and O are the first very short-lived products of the formamide discharge decomposition.

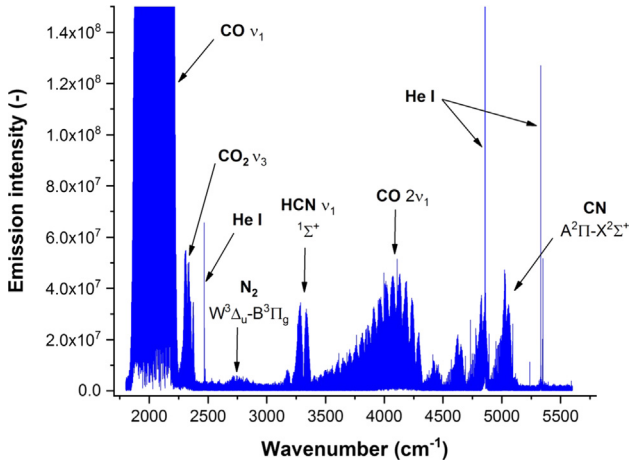

Fig. 3. Emission spectrum of formamide/N_2/H_2O/He glow discharge, 11 μs after the discharge pulse.

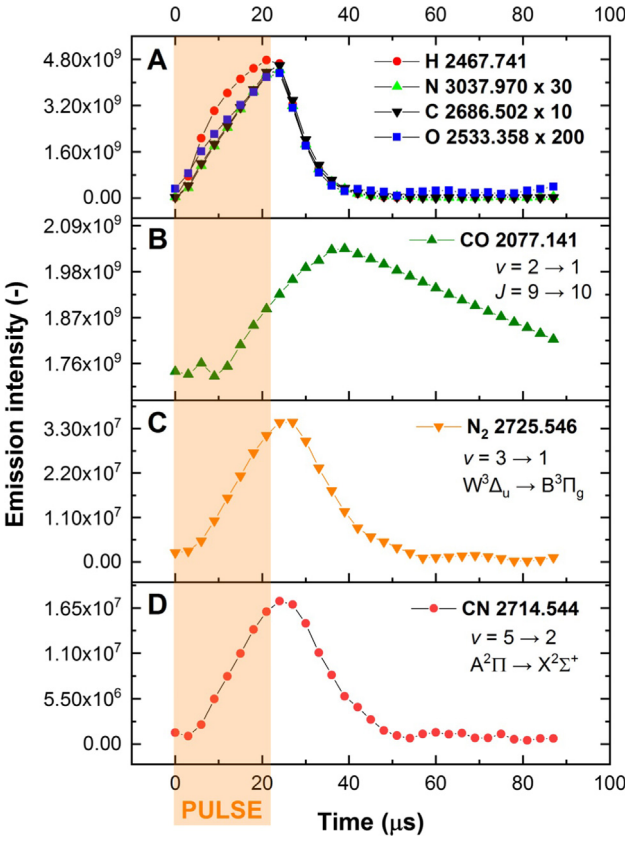

Fig. 4. Overall time profiles of selected species.

On the other hand, carbon monoxide is a long-living stable molecule, which discharge creation mechanism is depicted in panel B of Fig. 4. The maximum intensity of the CO emission is about 15 μs after the discharge pulse. Interesting fact is the CO emission is quenched at the beginning of the discharge pulse to the zero emission intensity. Excitation of the CO takes place during the pulse period and culminates about 15 μs after the pulse period.

Nitrogen, which can be seen in the panel C of Fig. 4, has the time profile shortly shifted to the afterglow period. By comparison of the time profiles of CO together with N_2 one can see the fast decay of the N_2 signal and simultaneous increase of CO emission intensity. This fact confirms the theory of energy transfer between N_2 and CO molecules via collisional excitations.

The panel D of Fig. 4 demonstrates the time profile of CN radical, similar to the profile of N_2. From our previous experiments we assume that CN plays the same role in the discharge as the excited molecule of N_2 and serves as a high energy intermediate for many other molecules like CO, CO_2 or HCN.

4.3. Rotational and vibrational temperatures of the discharge plasma

Temperature of the plasma is one of its important characteristics. Temperature generally describes the energetic distribution of particles in the plasma system. Furthermore, the plasma temperature can be divided into four groups – electron temperature T_{el}, vibrational temperature T_V, rotational temperature T_R and kinetic temperature T_σ. These temperatures can be characterized by following relation:

$$T_{el} > T_V > T_R \equiv T_\sigma \quad (12)$$

The distribution between the excited particles and the particles in the ground state is described by the excitation temperature T_{exc}.

Here we determined the rotational and vibrational temperatures of CO from the time-resolved spectra.

The emissivity of a rovibrational (or rovibronic) transition is given by Eq. (4) where the Einstein $A_{i\to f}$ coefficient is related to the line strength $S_{v'J',v}$ as follows

$$A_{if} = 16\frac{\pi^3\nu^3}{3h\varepsilon_0}\frac{S_{if}}{\left(2J'+1\right)}. \tag{13}$$

In the case of pure rotational-vibrational transitions, the rotational temperature can be estimated under the rigid-rotor approximation by the dependence:

$$\ln\left(\frac{I}{S_{J'J''}}\right) = \frac{-E_J^v}{kT_R} + Q_R \tag{14}$$

where I stands for the intensity, $S_{J'J''}$ is Hönl-London factor (defined as $S_{J'J''} = (J' + 1)$ for the R-branches, E_J^v is the energy of upper rotational level, k is Boltzmann constant, T_R stands for the rotational temperature and Q_R is a constant, which absorbs the vibrational Franck-Condon factor in the line strength.

Under the rigid rotor approximation for the rotational energy of the upper state

$$E_J^v = hcB_vJ(J+1), \tag{15}$$

for $\ln(I/S_{J'J''})$ we obtain

$$\ln\left(\frac{I}{S_{J'J''}}\right) = \frac{K}{T_R}J(J+1) + Q_R \tag{16}$$

where

$$K = -\frac{hcB_{v'}}{k}, \tag{17}$$

h is Planck constant, c is the speed of light in vacuum, $B_{v'}$ is a rotational constant for the upper v-state, k is Boltzmann constant and K stands for the slope of the linear regression.

When applying the linear regression on the dependence in Eq. (16), see Fig. 5, the rotational temperature is then obtained from the slope of such regression by:

$$T_R = -\frac{hcB_{v'}}{Kk} \tag{18}$$

As can be seen in Fig. 5, the rotational temperature was calculated to be T_R = 555 ± 3 K.

The vibrational temperature of the discharge plasma can be reconstructed in a similar way applying a double-harmonic approximation (harmonic potential and linear dipole moment) to the intensities of the $\Delta v = 1$ bands, see Fig. 6. Under this approximation, the vibrational band strength of a $v+1 \to v$ transition is simplified by.

$$S_{v+1,v} = \mu_1(v+1), \tag{19}$$

where μ_1 is the first derivative of the dipole moment with respect to the vibrational, normal mode coordinate.

The vibrational temperature can be then estimated by plotting the dependence

$$\ln\left[\frac{I}{\nu^3(v'+1)}\right] = KE_{v'} + Q_V \tag{20}$$

in terms of $E_{v'}$, where I stands for the intensity, ν is the wavenumber of an edge of the selected band (wavenumber of the most intense line), v' is the vibrational quantum number of an upper energy state, $K = -\frac{hc}{kT_V}$ is the slope of the linear regression, $E_{v'}$ is the energy of an upper v-state and Q_V is a constant. Applying the linear regression, it is possible to derive the vibrational temperature by:

$$T_V = -\frac{hc}{kK} \tag{21}$$

The vibrational temperature was calculated as T_V = 7194 ± 270 K. The rotational quantum number was fixed to J = 10 → 9.

4.4. The band shape of the first overtone of CO

Using similar approximation to the first overtone band of CO, △v = 2, for the vibrational band strength we obtain.

$$S_{v+2,v} = \mu_2(v+1)(v+2), \tag{22}$$

where μ_2 is the quadratic expansion coefficient of the dipole moment with respect to the vibrational mode coordinate. Combining it with the Boltzmann population of the upper vibrational states based on the harmonic oscillator, the vibrational intensity is given by.

$$I_{v+2,v} = P_v e^{\frac{-c_2\tilde{\omega}\left(v+\frac{1}{2}\right)}{T_V}}(v+1)(v+2), \tag{23}$$

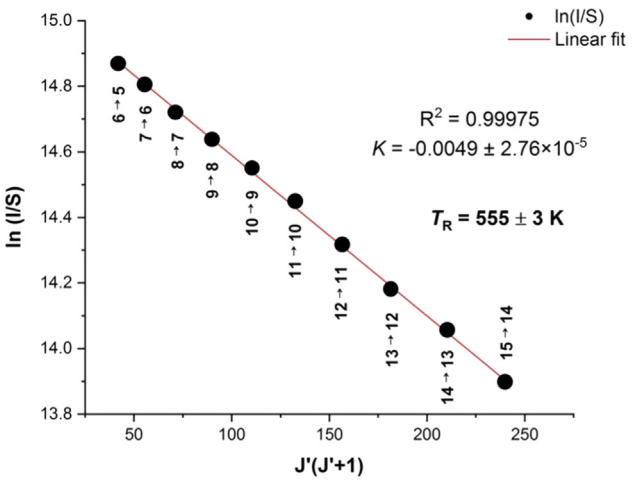

Fig. 5. Determination of the rotational temperature of CO molecule (J-transitions specified) for v = 2 → 1 vibrational transition.

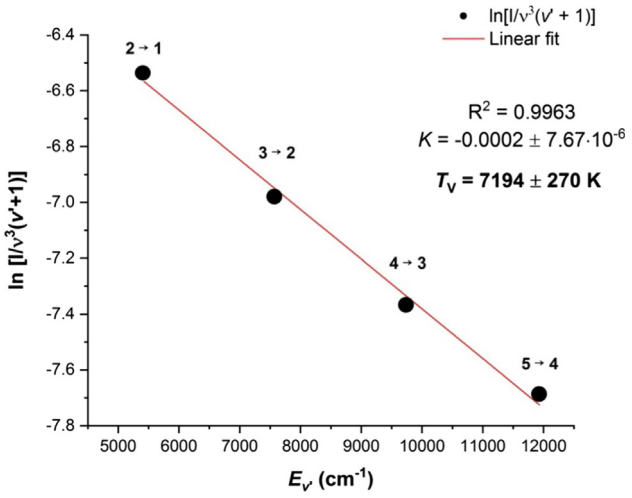

Fig. 6. Determination of the vibrational temperature of the discharge plasma (v-transitions specified).

where P_v is a constant, $\tilde{\omega}$ is the harmonic constant and c_2 is the second radiation constant (K/cm^{-1}). This is illustrated in Fig. 7, where both vibrational dependences as well as their combination are shown then explains the resulting band shape of CO's first overtone.

While the Boltzmann population of the upper vibrational states of CO exponentially decreases with increasing vibrational quantum number (Panel A), the line strength of individual vibrational states (Panel B) follows a quadratic growth with v. The resulting intensities of the vibrational △v = 2 band of CO forms a maximum at around v = 4, which is close enough to the experimental overtone spectrum of CO, see Fig. 8.

4.5. Non-LTE

The methods in Section "Non-LTE modelling" were used for each of the fragment molecules in the formamide spectrum, using each as necessary to obtain the best fit. The description of the results for each molecule are in the subsections below. As Exocross' units for emission intensities, I, are in erg/(str molecule), the results needed rescaled to match experiment, such that:

$$I_{(\mathrm{exp})} = \frac{I_{(\mathrm{ExoCross})}}{hc\,\tilde{\nu}} \tag{24}$$

where h (Planck's constant), c (speed of light) and $\tilde{\nu}$ (wavenumber) are all in units of cgs.

4.6. CO

The CO emission was plotted via the bi-temperature approach using the ExoMol line list by Li et al. [79]. The individual Δv = 2 bands (v = 0...17) at 4000 cm^{-1} were filtered and are plotted in Fig. 8 to show the different transitions and how they compare to experiment. For the upper states involved in these emission transitions the same rotational and vibrational temperatures are assumed, T_R = 555 K, T_v = 7194 K. The emission cross sections were generated using the Voigt line profile with the half-width-half-maximum (HWHM) of 0.02 cm^{-1}. The bi-temperature calculations were scaled by 230 to match experimental intensities.

The 1D effective approach can be used to achieve similar results, and are shown in Fig. 9 below. The parameters r_0 = 1.24Å and ω_0 = 850.0 cm^{-1} were used to model the "fragment" CO, along with a rotational temperature of 555 K. The "gas phase" and "fragment" parameters used in the calculations are shown in Table 1 below, and the resulting population densities are included in Table A1. The 1D results were scaled by 130 to match with the experimental intensities. A zoom of the bi-temperature vs 1D plot is shown in Fig. 10, which shows the excellent agreement achieved using the two methods.

4.7. N_2

The spectrum of N_2 calculated using the ExoMol line list WCCRMT [77] was matched by using the bi-temperature non-LTE model. The $W^3\Delta$-$B^3\Pi_g$ Δv = 2 bands are the ones responsible for the transitions seen in the dissociation spectrum between 2300 and 3100 cm^{-1}. The best matches to the experimental results are shown in Fig. 11 for the 2200–3800 cm^{-1} and the 3800–5000 cm^{-1} region. Calculations were performed in emission with T_R = 555 K, T_V = 6800 K, resolution = 0.01 cm^{-1}, Voigt line profile, and a HWHM = 0.017 cm^{-1}. The scaling factors are 200 for the W-B band and 1400 for the B-W and B-A bands.

As N_2 is not a plausible fragment to dissociate directly from formamide, owing to formamide only having one nitrogen atom, it is either a secondary product formed via an intermediate, or a result of the nitrogen gas used in the experiment being excited. The discharge spectrum of nitrogen has been studied for its non-LTE atmospheric properties owing to its excitation in events such as aurorae and lightnings [77]. Therefore, the N_2 results have not been modelled using the 1D approach as using a "fragment" and "gas phase" comparison would make little physical sense.

4.8. CN

The spectrum of CN was matched by using the bi-temperature method using the MoLLIST [80] ExoMol line list. The $X^2\Sigma^+$-$A^2\Pi$ band is shown in Fig. 12 below. Calculations were performed in emission with T_R = 555 K, T_V = 7000 K, resolution = 0.01 cm^{-1}, Voigt line profile, and a HWHM = 0.02 cm^{-1}. The bi-temperature results did not need scaling.

The 1D effective approach can also be used with CN to achieve excellent results compared to the bi-temperature approach, and are shown in Fig. 13 below. The parameters r_0 = 1.279Å and ω_0 = 898.0 cm^{-1} were used for the fragment CN, along with a rotational temperature of 555 K. The "gas phase" and "fragment" parameters used in the calculations are shown in Table 2 below, and the resulting population densities are included in Table A1. The 1D results were scaled by 0.6 to match with the experimental intensities. A zoom of the bi-temperature vs 1D plot is shown in Fig. 14, which shows the excellent agreement achieved using the two methods.

4.9. CO_2

Emission spectra of CO_2 assuming LTE and the kinetic temperature T = 555 K are shown in Fig. 16, corresponding to the ν_3 (CO_2) regions of the experimental spectra.

The CO_2 spectrum was simulated using the ExoMol line lists UCL-4000 (CO_2) [84]. The spectrum agrees well with the experi-

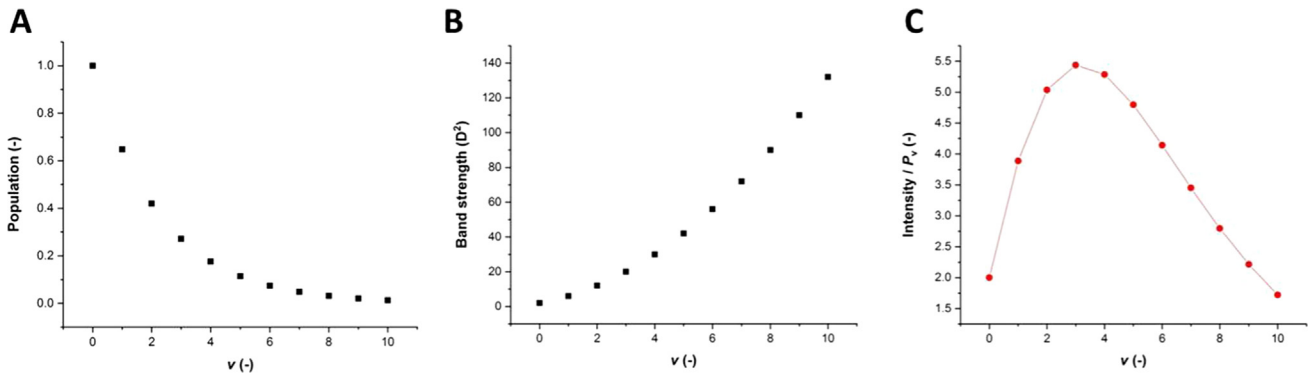

Fig. 7. Explanation of the shape of CO's first overtone band.Panel A – Boltzmann vibrational population for individual vibrational states.Panel B – Line strength of individual vibrational states for △v = 2.Panel C – Resulting intensity of individual vibrational states. The vibrational temperature T_v is 7194 K and the harmonic constant $\tilde{\omega}$ is 2100 cm^{-1}.

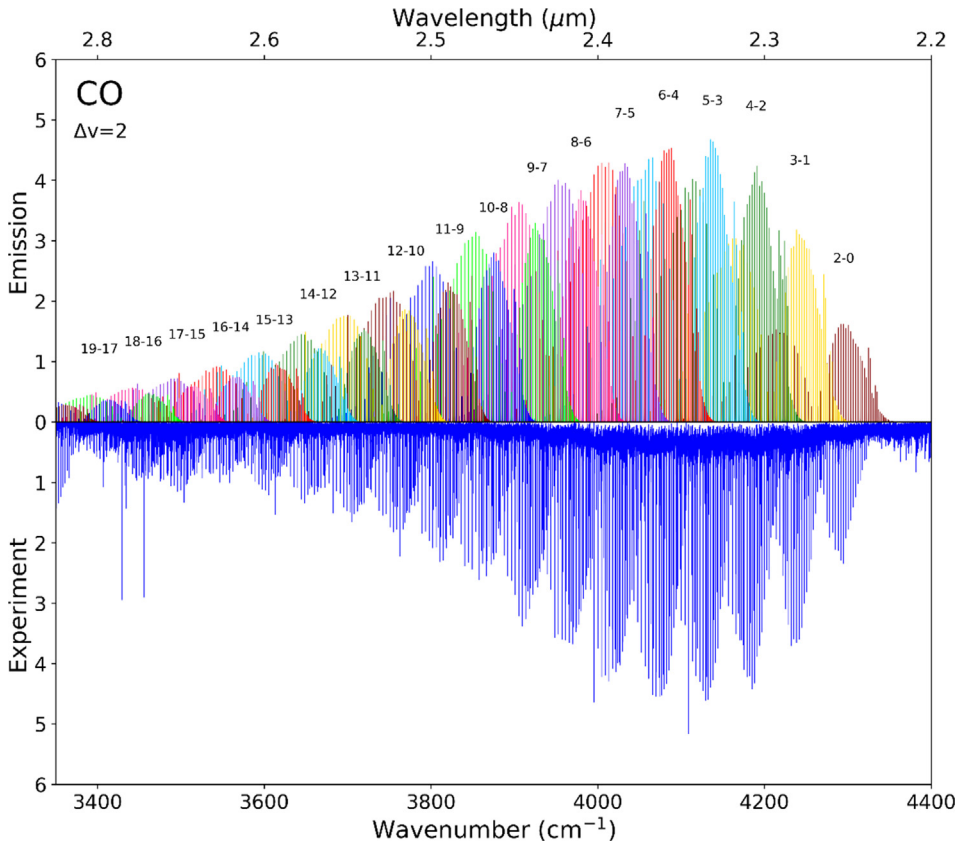

Fig. 8. The bi-temperature non-LTE emission spectra of CO, showing the $\Delta v = 2$ band and the individual transitions, T_v = 7194 K and T_R = 555 K. A scaling factor of 230 was used for the computed intensities. The ExoMol line list by Li et al. [79] was used.

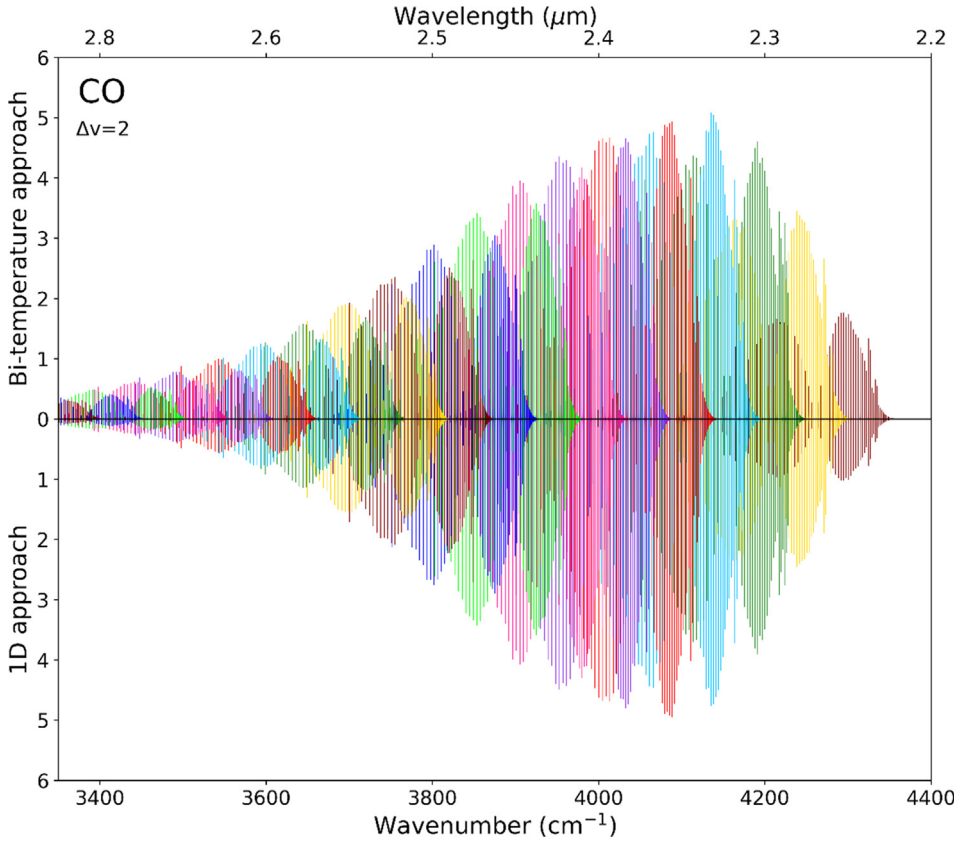

Fig. 9. The bi-temperature (top) versus 1D (bottom) calculations for the emission of CO.

Table 1
The gas phase and fragment parameters used in the 1D modelling of CO.

Molecule	CO	
	r, Å	$\tilde{\omega}$, cm^{-1}
Gas Phase	1.128 [86]	2170 [87]
Fragment	1.24	850

ment, however a part of the ν_3 band of CO_2 is not present in the experimental spectrum. We attribute this effect to the self-absorption via the fundamental band ν_3 (00011 in the HITRAN notation). Within our experimental setup, the glow discharge in the discharge cell is not spread over the whole volume of the discharge tube. Hence, a small amount of cold gas, obstructing the beam from the glow discharge, exists between the window and the discharge itself. Cold CO_2 is a strong absorber and the passing emission light is partially absorbed. The final effect is that the fundamental ν_3 band is missing in the formamide emission spectrum. Therefore, self-absorption of CO_2 occurs. Fig. 15 describes the self-absorption in detail.

The blue spectrum in Fig. 15 represents a standard formamide mixture emission spectrum. As can be clearly seen, the shape of the CO_2 emission band in this 2240–2400 cm^{-1} spectral range does

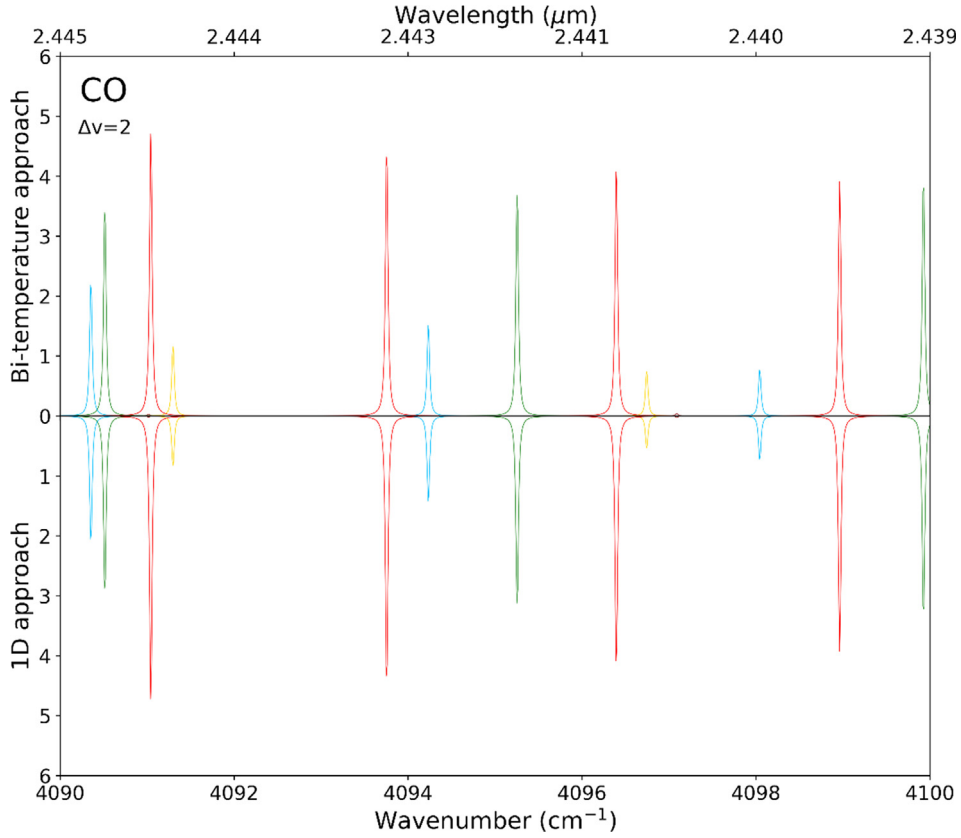

Fig. 10. Zoom of the bi-temperature (top) vs 1D (bottom) plot, showing the excellent agreement between the two methods.

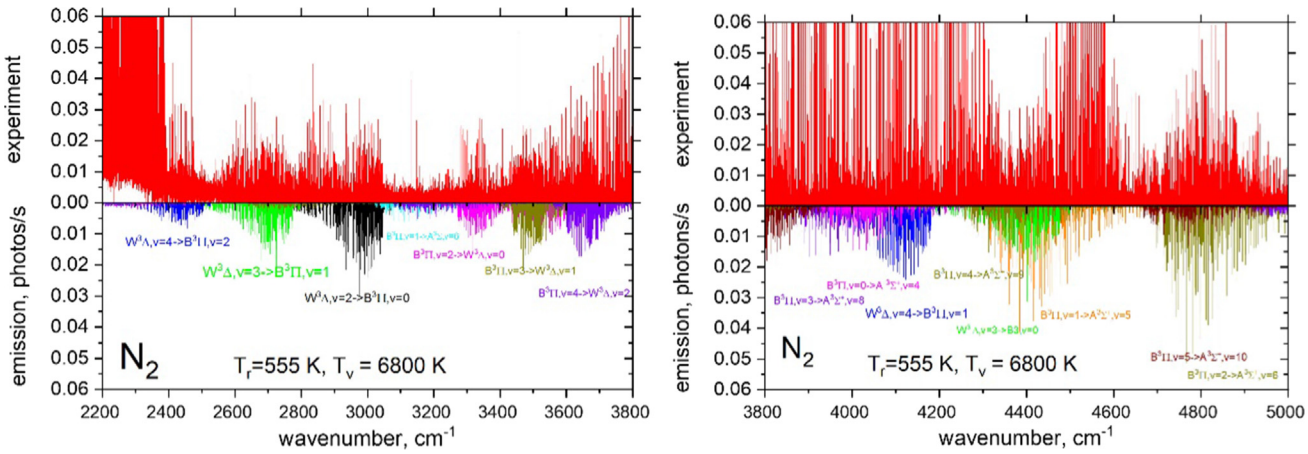

Fig. 11. Experiment (red) versus bi-temperature (multicoloured) modelling of the N_2 spectra between 2200 and 3800 cm^{-1} (left panel) and 3800–5000 cm^{-1} (right panel). The theoretical spectrum corresponds to the non-LTE combination of T_R = 555 K and T_v = 6800 K and the Voigt line profile with HWHM = 0.0017 cm^{-1}. The WCCRMT [77] line list was used.

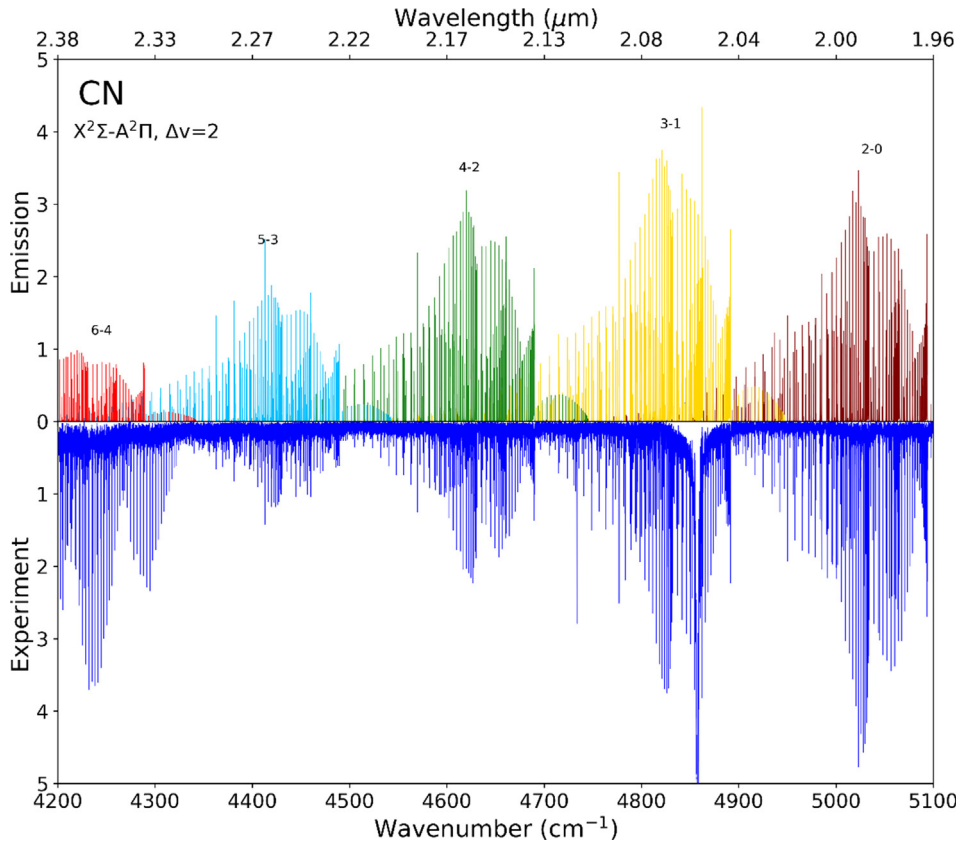

Fig. 12. The bi-temperature non-LTE emission spectra of CN, showing the $X^2\Sigma^+$-$A^2\Pi$ $\Delta v = 2$ band and the individual transitions, T_v = 7000 K and T_R = 555 K. CN scaling factor: 1. The line list MoLLIST [80,88] was used.

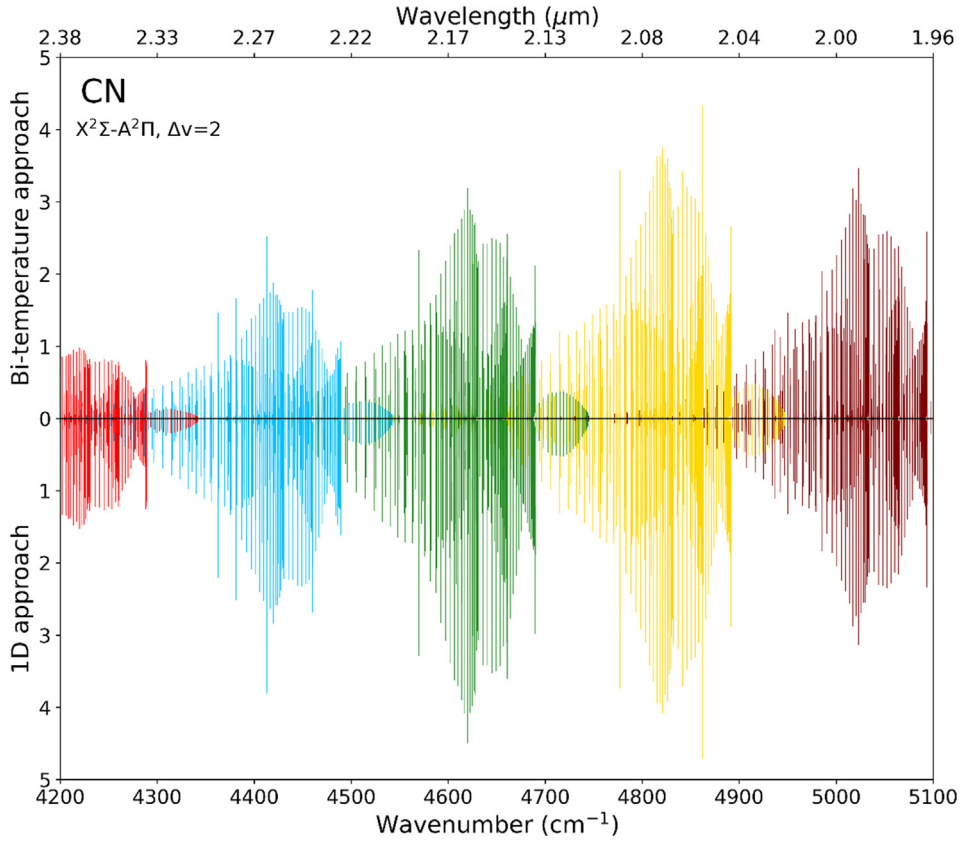

Fig. 13. The bi-temperature (top) versus 1D (bottom) calculations for the emission of CN. Scaling factors of 1 and 0.6 were used for the bi-temperature and 1D-harmonic approaches, respectively. The MoLLIST [80,88] line list was used.

Table 2
The gas phase and fragment parameters used in the 1D modelling of CN.

Molecule	CN	
	r, Å	ω, cm^{-1}
Gas Phase	1.1384 [87]	1117.72 [87]
Fragment	1.279	898

not match the shape of the CO_2 absorption spectrum (red). This is owing to the aforementioned strong self-absorption of CO_2 bands by cold gas. The blue spectrum of the formamide mixture discharge is therefore a combination of two different effects – absorption and emission together. The absorption spectrum of the fundamental band eliminates the emission transitions, and a part of the emission spectrum which belongs to the ν_3 band is missing in our experimental formamide spectrum.

The pure emission spectrum of CO_2 (long discharge cell) can be seen in Panel B of Fig. 15 (green spectrum). Here, only negligible self-absorption occurs (lines below the baseline, negative values).

The experimental spectrum in Fig. 16 can be matched to the hot ν_2 + ν_3-ν_2 (01111–01101) and 2ν_3-ν_3 (00021–00011) hot bands of CO_2, as well as to the $2v_2 + 2v_3 - 2v_2$ (10022–01101 and 02221–01101) (lower display, plotted in green, blue and pink) spectrum. The 2ν_3-ν_3 band is an especially important feature of non-LTE CO_2 within the Martian atmosphere [89] where the overpopulation of the upper state is caused by solar radiation pumping at 2.7 μm, which subsequently emit to produce the feature at 2127 cm^{-1} as seen in Fig. 16 [90]. If the intensity of the $v_2 + v_3 - v_2$ hot band is reproduced by the (LTE) temperature of T = 555 K comparing to the intensities of the fundamental band v_3, the $2v_3 - v_3$ and $2v_2 + 2v_3 - 2v_2$ hot bands require higher vibrational temperature of about 700 K.

Calculations were performed in emission with T_R = 555, resolution = 0.01 cm^{-1}, Voigt line profile, and a HWHM = 0.02 cm^{-1}. The intensity of the theoretical results was scaled by 23 to match the intensity of the experimental results.

4.10. HCN

An emission spectrum of HCN assuming LTE and the kinetic temperature T = 555 K was computed using the ExoMol line list Harris [82,83] and is shown in Fig. 17, corresponding to the ν_1 (HCN) regions of the experimental spectra.

In the case of HCN, due to a higher level of contamination by other spectral lines of other species (N_2, H_2O), it is not that clear to see the hot band ν_1 + ν_2-ν_2. However these lines can be easily found when zoomed on individual lines, see Fig. 18.

The reconstruction of the rotational emission intensities of the HCN band υ_1 is illustrated in the upper part of Fig. 17 using the blue lines in the background, computed using T_R = 555 K.

5. Conclusion

We demonstrated the time-resolved infrared emission spectra of formamide-water-nitrogen mixture, processed in the glow discharge with helium as a buffer gas. We also discussed the possibilities of mutual energy transfer in the discharge system. The system contains many radicals as well as other neutral species. According to our time profile data, CN radical and especially molecular nitrogen serve as an energy mediator in the whole system, allowing other species to be excited to various energy levels. The first and fastest energy mediators were found to be atoms (H, C, N, O or even atomic helium), which most likely serve as an agent in the energy transfer between the discharge itself and molecular species.

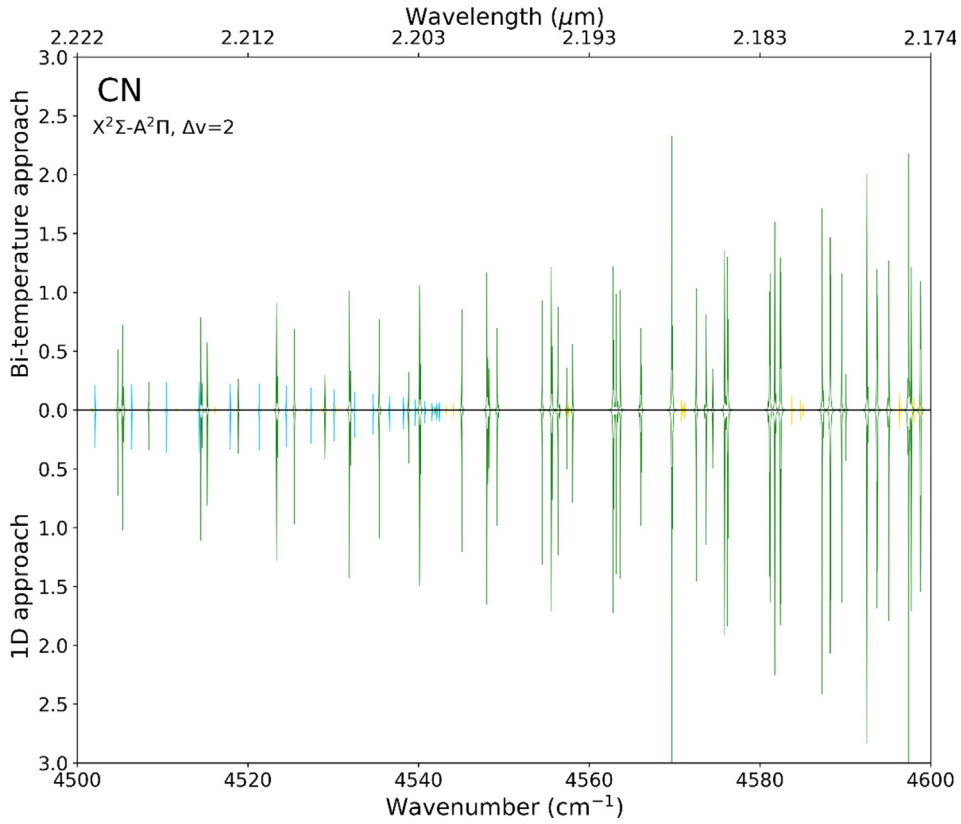

Fig. 14. Zoom of the bi-temperature (top) vs 1D (bottom) plot of CN, showing the excellent agreement between the two methods.

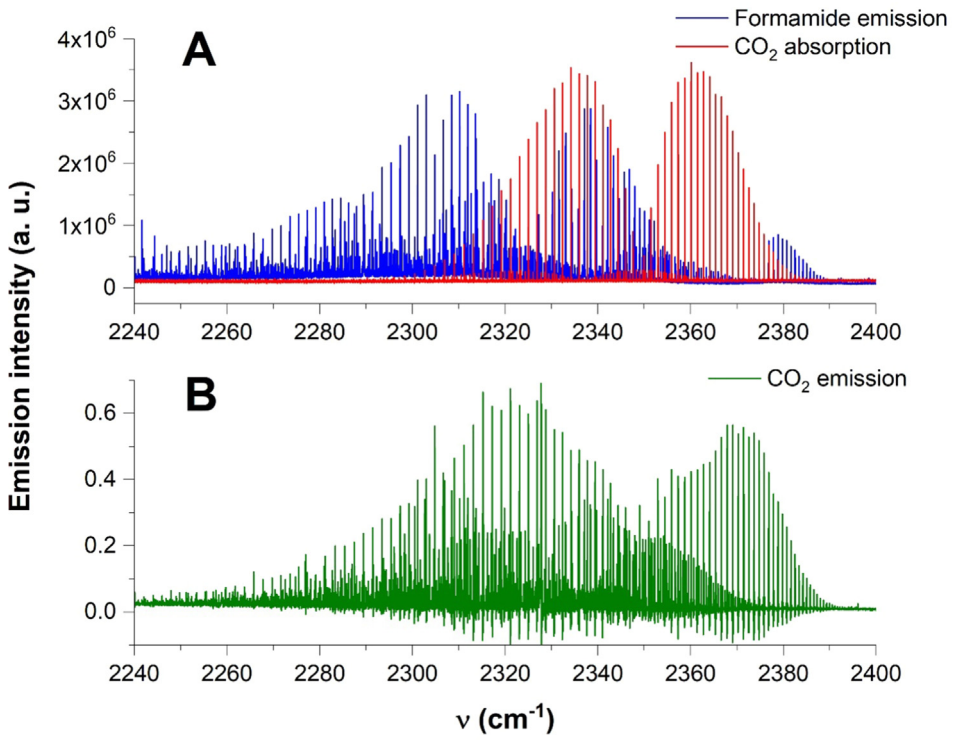

Fig. 15. Panel A – formamide emission together with CO_2 ν_3 absorption spectrum (red) Panel B – CO_2 emission spectrum (long discharge cell).

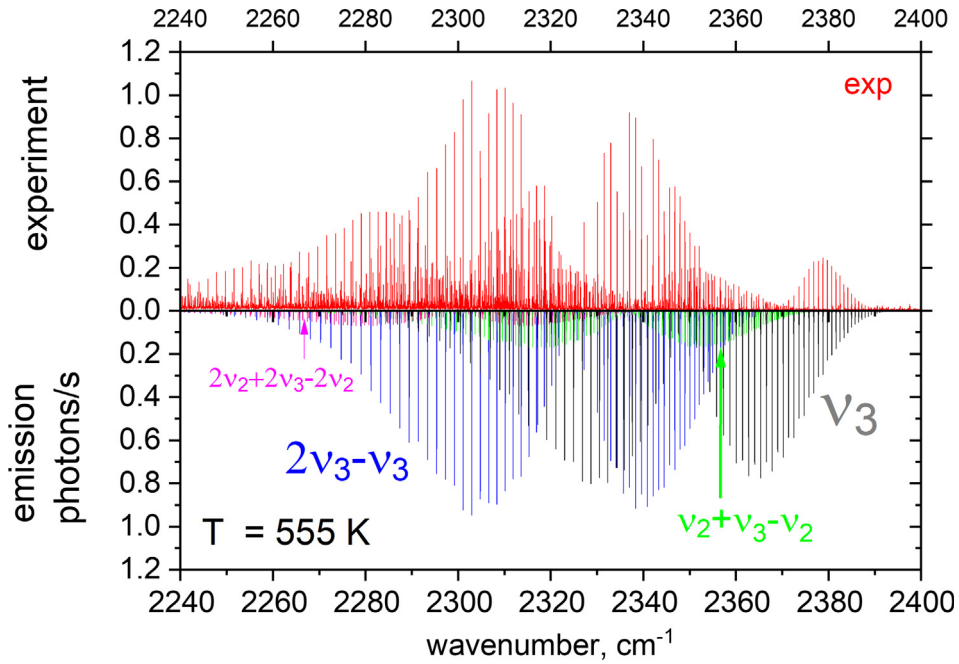

Fig. 16. Experiment (top) against theoretical emission (bottom) CO_2 spectrum. A scaling factor of 23 was used to match the calculated ν_3 band (00001 in the HITRAN notation) to experimental intensities. We attribute the self-absorption mechanism to the disappearance of the experimental ν_3 spectrum. The line list UCL-4000 [84] was used, where the rotational temperature of T_R = 555 K was assumed.

By the use of time profiles, we demonstrated that CO can be easily excited via collisional interactions with nitrogen. Nitrogen's energy depletion time curve exhibits almost precisely opposite trend to CO's one, which supports this theory.

In our opinion, the above spectroscopic measurements show that the main dissociation products, such as CN radical, vibrationally–rotationally highly excited CO and hydrogen cyanide may provide a key to understand how large organic molecules could be formed in the course of a high-energy–density event.

Lastly, we presented our new non-LTE multi-molecule model of the whole formamide discharge spectrum. CO and CN were modelling using both a bi-temperature and a 1D harmonic approxima-

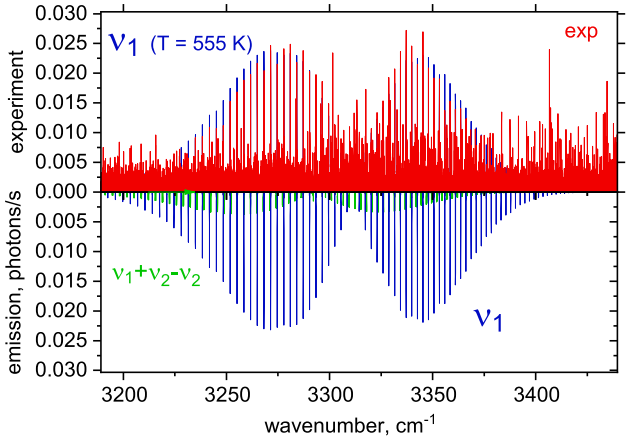

Fig. 17. Experiment (top) against theoretical emission (bottom) HCN spectrum. A scaling factor of 48 was used to match calculated results to experimental intensities. The ExoMol line list Harris [82,83] was used in simulations assuming T_R = 555 K. The theoretical ν_1 band is also shown (blue) in the experimental (top) part of the spectrum as reference.

tion, of which an excellent agreement to experiment was achieved with both methods; N_2 was modelling using the bi-temperature approach; HCN was modelled using a single temperature approach with visible hot bands. The CO_2 spectrum is affected by complex non-LTE, which cannot be described by a single vibrational temperature. As the spectrum for every molecule was calculated independently, the spectra had to be scaled when plotting on the same graph. Scaling factors of 230 and 130 were used for bi-temperature and 1D approximation of CO, respectively; 1 and 0.6 were used for bi-temperature and 1D approximation of CN, respectively; a scaling factor of 23 was used for the band-scaling approach of CO_2; and a scaling factor of 48 was used for the HCN calculations. The detailed theoretical analysis highlighted the presence of self-absorption within the ν_3 CO_2 band which can be attributed to the presence of a small volume of cold gas within the experimental setup, obstructing the emission light beam. The CO_2 self-absorption produces an uncommon CO_2 band shape and may play an important role in the spectroscopic analysis of exoplanetary atmospheres.

CRediT authorship contribution statement

Adam Pastorek: Investigation, Writing – original draft, Visualization, Conceptualization. **Victoria H.J. Clark:** Writing – original draft, Software, Formal analysis, Visualization. **Sergei N. Yurchenko:** Software, Data curation, Writing – review & editing, Funding acquisition. **Martin Ferus:** Funding acquisition. **Svatopluk Civiš:** Supervision, Funding acquisition, Writing – review & editing, Methodology, Conceptualization.

Declaration of Competing Interest

The authors declare that they have no known competing financial interests or personal relationships that could have appeared to influence the work reported in this paper.

Acknowledgments

This work was funded by grant no. CZ.02.1.01/0.0/0.0/16_019/0000778 alias "ERDF/ESF Centre of Advanced Applied Sciences", UK research councils EPSRC under grant EP/N509577/1 and STFC, under grant ST/R000476/1. The theoretical work made extensive use of the STFC DiRAC HPC facility supported by BIS National E-infrastructure capital grant ST/J005673/1 and STFC grants ST/H008586/1 and ST/K00333X/1. We thank the European Research Council (ERC) under the European Union's Horizon 2020 research and innovation programme through Advance Grant number 883830. MF acknowledges grant of the Czech Science Foundation no. 21-11366S.

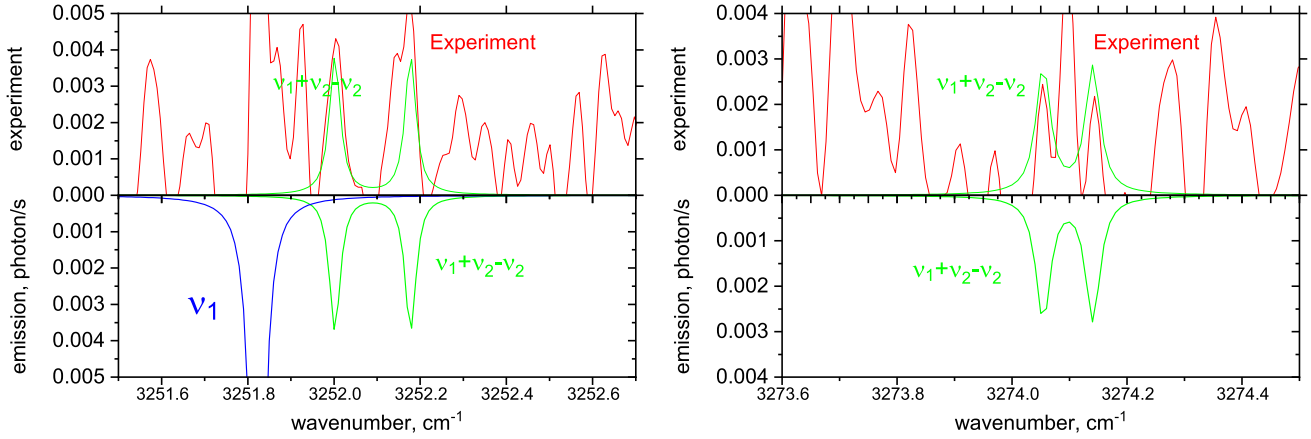

Fig. 18. Zoom of the HCN spectrum to show the match between theory (T_R = 555 K) and experiment for regions 3273.6–3274.6 cm^{-1} (left) and 3251.5–3252.7 cm^{-1} (right).

Appendix

See Table A1.

Table A1
The vibrational populations used in the 1D harmonic modelling of the CO and CN emission spectrum.

υ	Population (CO)	Population (CN)
0	1.910956E−01	2.325315E−01
1	1.666362E−01	1.934373E−01
2	1.637333E−01	1.748927E−01
3	1.323697E−01	1.309887E−01
4	1.043470E−01	9.484237E−02
5	7.679794E−02	6.418863E−02
6	5.500256E−02	4.213688E−02
7	3.798936E−02	2.667416E−02
8	2.567350E−02	1.649570E−02
9	1.694891E−02	9.961864E−03
10	1.099961E−02	5.908609E−03
11	7.019108E−03	3.444594E−03
12	4.418334E−03	1.979682E−03
13	2.745248E−03	1.122665E−03
14	1.686796E−03	6.293159E−04
15	1.025625E−03	3.489801E−04
16	6.178409E−04	1.916659E−04
17	3.689616E−04	1.043256E−04
18	2.186034E−04	5.632320E−05
19	1.285638E−04	3.017657E−05
20	7.509723E−05	1.605444E−05
21	4.358644E−05	8.485072E−06
22	2.514759E−05	4.457048E−06
23	1.442804E−05	2.327706E−06
24	8.234507E−06	1.209075E−06
25	4.676391E−06	6.248178E−07
26	2.643324E−06	3.213320E−07
27	1.487512E−06	1.644993E−07
28	8.335710E−07	8.384694E−08
29	4.652482E−07	4.256138E−08
30	2.586853E−07	2.151971E−08

References

[1] A.I. Oparin, The Origin of Life, Macmillan Company, New York, 1938, viii p 2.
[2] S.L. Miller, A production of amino acids under possible primitive earth conditions, Science (80-.) 117 (3046) (1953) 528–529.
[3] S.L. Miller, H.C. Urey, Organic compound synthesis on the primitive earth, Science (80-.) 130 (1959) 245–251.
[4] N. Balucani, Elementary reactions and their role in gas-phase prebiotic chemistry, Int. J. Mol. Sci. 10 (2009) 2304–2335.
[5] A. Bar-Nun, A. Shaviv, Dynamics of the chemical evolution of Earth's primitive atmosphere, Icarus 24 (2) (1975) 197–210.
[6] M. Ferus, I. Matulkova, L. Juha, S. Civis, Investigation of laser-plasma chemistry in CO-N_2-H_2O mixtures using ^{18}O labeled water, Chem. Phys. Lett. 472 (2009) 14–18.
[7] S. Civiš et al., Amino acid formation induced by high-power laser in CO_2 / CO–N_2–H_2O gas mixtures, Chem. Phys. Lett. 386 (2004) 169–173.
[8] H.L. Barks, R. Buckley, G.A. Grieves, E. Di Mauro, N.V. Hud, T.M. Orlando, Guanine, adenine, and hypoxanthine production in uv-irradiated formamide solutions: relaxation of the requirements for prebiotic purine nucleobase formation, ChemBioChem 11 (9) (2010) 1240–1243.
[9] R. Saladino et al., Meteorite-catalyzed syntheses of nucleosides and of other prebiotic compounds from formamide under proton irradiation, Proc. Natl. Acad. Sci. 112 (2015) E2746–E2755.
[10] R. Saladino et al., Proton irradiation: a key to the challenge of N-glycosidic bond formation in a prebiotic context, Sci. Rep. 7 (2017) 14709.
[11] A. Pastorek et al., Primordial radioactivity and prebiotic chemical evolution: effect of γ radiation on formamide-based synthesis, J. Phys. Chem. B 124 (2020) 8951–8959.
[12] R. Saladino, C. Crestini, G. Costanzo, E. DiMauro, On the prebiotic synthesis of nucleobases, nucleotides, oligonucleotides, Pre-RNA and Pre-DNA Molecules, in: Prebiotic Chemistry, vol. 259, Springer-Verlag, 2005, pp. 29–68.
[13] Hiroshi Yamada, Toshihiko Okamoto, A one-step synthesis of purine ring from formamide, Chem. Pharm. Bull. (Tokyo) 20 (3) (1972) 623–624.
[14] H. Yamada, M. Hirobe, K. Higashiyama, H. Takahashi, K.T. Suzuki, Detection of carbon-13-nitrogen-15 coupled units in adenine derived from doubly labeled hydrogen cyanide or formamide, J. Am. Chem. Soc. 100 (1978) 4617–4618.
[15] A. Pastorek et al., Prebiotic synthesis at impact craters: the role of Fe-clays and iron meteorites, Chem. Commun. 55 (2019) 10563–10566.
[16] M. Ferus et al., High energy radical chemistry formation of hcn-rich atmospheres on early earth, Sci. Rep. 7 (2017) 6275.
[17] J. Xu et al., A prebiotically plausible synthesis of pyrimidine beta-ribonucleosides and their phosphate derivatives involving photoanomerization, Nat. Chem. 9 (2017) 303–309.
[18] J.D. Sutherland, Studies on the origin of life - the end of the beginning, Nat. Rev. Chem. 1 (2017).
[19] S. Civiš et al., The origin of methane and biomolecules from a CO_2 cycle on terrestrial planets, Nat. Astron. 1 (2017) 721–726.
[20] J.D. Sutherland, The origin of life-out of the blue, Angew. Chemie – Int. Ed. 55 (1) (2016) 104–121.
[21] M.W. Powner, J.D. Sutherland, Prebiotic chemistry: a new modus operandi, Philos. Trans. R. Soc. B Biol. Sci. 366 (2011) 2870–2877.
[22] M. Powner, J. Sutherland, J. Szostak, The origins of nucleotides, Synlett 2011 (14) (2011) 1956–1964.
[23] J.E. Šponer et al., Prebiotic synthesis of nucleic acids and their building blocks at the atomic level - merging models and mechanisms from advanced computations and experiments, Phys. Chem. Chem. Phys. 18 (2016) 20047–20066.
[24] M. Ferus et al., High-energy chemistry of formamide: a unified mechanism of nucleobase formation, Proc. Natl. Acad. Sci. 112 (2014) 657–662.
[25] M. Ferus et al., Formation of nucleobases in a Miller-Urey reducing atmosphere, Proc. Natl. Acad. Sci. 114 (2017) 4306–4311.
[26] L. Rotelli, J.M. Trigo-Rodríguez, C.E. Moyano-Cambero, E. Carota, L. Botta, E. Di Mauro, R. Saladino, The key role of meteorites in the formation of relevant prebiotic molecules in a formamide/water environment, Sci. Rep. 6 (1) (2016).
[27] R. Saladino, G. Botta, S. Pino, G. Costanzo, E. Di Mauro, From the one-carbon amide formamide to RNA all the steps are prebiotically possible, Biochimie 94 (7) (2012) 1451–1456.
[28] R. Saladino, G. Botta, B.M. Bizzarri, E. Di Mauro, J.M. Garcia Ruiz, A global scale scenario for prebiotic chemistry, Biochemistry 55 (19) (2016) 2806–2811.
[29] W.A. Schutte et al., Weak ice absorption features at 7.24 and 7.41 μm in the spectrum of the obscured young stellar object W 33A, Astron. Astrophys. 343 (1999) 966–976.
[30] C. Kahane, C. Ceccarelli, A. Faure, E. Caux, detection of formamide, the simplest but crucial amide in a solar-type protostar, Astrophys. J. 763 (2013) L38.
[31] N. Biver et al., Complex organic molecules in comets C/2012 F6 (Lemmon) and C/2013 R1 (Lovejoy): Detection of ethylene glycol and formamide, Astron. Astrophys. 566 (2014) L5.
[32] F. Goesmann, H. Rosenbauer, J.H. Bredehöft, M. Cabane, P. Ehrenfreund, T. Gautier, C. Giri, H. Krüger, L. Le Roy, A.J. MacDermott, S. McKenna-Lawlor, U.J. Meierhenrich, G.M.M. Caro, F. Raulin, R. Roll, A. Steele, H. Steininger, R. Sternberg, C. Szopa, W. Thiemann, S. Ulamec, Organic compounds on comet 67P/Churyumov-Gerasimenko revealed by COSAC mass spectrometry, Science (80-. 349 (6247) (2015).
[33] R. Saladino, C. Crestini, F. Ciciriello, E. Di Mauro, G. Costanzo, Origin of informational polymers differential stability of phosphoester bonds in ribomonomers and ribooligomers, J. Biol. Chem. 281 (2006) 5790–5796.
[34] J.L. Bada, How life began on earth: a status report, Earth Planet. Sci. Lett. 226 (1–2) (2004) 1–15.
[35] J.E. Sponer et al., Emergence of the first catalytic oligonucleotides in a formamide-based origin scenario, Chem. Eur. J. 22 (2016) 3572–3586.
[36] P.H. Abelson, Amino acids formed in primitive atmospheres, Science 124 (1956) 935–941, https://doi.org/10.1126/science.124.3228.935.
[37] B.M. Rode, Peptide and the origin of life, Peptides 20 (1999) 773–786.
[38] A.M. Saitta, F. Saija, Miller experiments in atomistic computer simulations, Proc. Natl. Acad. Sci. U. S. A. 111 (38) (2014) 13768–13773.
[39] S. Miyakawa, H.J. Cleaves, S.L. Miller, The cold origin of life: A. Implications based on the hydrolytic stabilities of hydrogen cyanide and formamide, Orig. Life Evol. Biosph. 32 (2002) 195–208.
[40] M. Ferus, P. Kubelík, S. Civiš, Laser spark formamide decomposition studied by FT-IR spectroscopy, J. Phys. Chem. A 115 (44) (2011) 12132–12141.
[41] M. Ferus et al., On the road from formamide ices to nucleobases: IR-spectroscopic observation of a direct reaction between cyano radicals and formamide in a high-energy impact event, J. Am. Chem. Soc. 134 (2012) 20788–20796.
[42] S. Civiš, P. Kubelík, M. Ferus, Time-resolved fourier transform emission spectroscopy of He/CH_4 in a positive column discharge, J. Phys. Chem. A 116 (2012) 3137–3147.
[43] M. Ferus, I. Matulková, L. Juha, S. Civiš, Investigation of laser–plasma chemistry in CO–N_2–H_2O mixtures using ^{18}O labeled water, Chem. Phys. Lett. 472 (2009) 14–18.
[44] S. Civiš, T. Šedivcová-Uhlíková, P. Kubelík, K. Kawaguchi, Time-resolved Fourier transform emission spectroscopy of $A^2\Pi$-$X^2\Sigma^+$ infrared transition of the CN radical, J. Mol. Spectrosc. 250 (2008) 20–26.
[45] V. Horká, S. Civiš, V. Špirko, K. Kawaguchi, The infrared spectrum of CN in its ground electronic state, Collect. Czechoslov. Chem. Commun. 69 (1) (2004) 73–89.
[46] E. Dudás et al., Higherature hypersonic Laval nozzle for non-LTE cavity ringdown spectroscopy, J. Chem. Phys. 152 (2020).
[47] V.H.J. Clark, S.N. Yurchenko, Modelling the non-local thermodynamic equilibrium spectra of silylene SiH_2, Phys. Chem. Chem. Phys. 23 (20) (2021) 11990–12004.
[48] F.F.S. Van Der Tak, J.H. Black, F.L. Schöier, D.J. Jansen, E.F. Van Dishoeck, A computer program for fast non-LTE analysis of interstellar line spectra with

diagnostic plots to interpret observed line intensity ratios, Astron. Astrophys. 468 (2007) 627–635, https://doi.org/10.1051/0004-6361:20066820.
[49] M. Carlsson, A computer program for solving multi-level non-LTE radiative transfer problems in moving or static atmospheres, in: Physics of Formation of FeII Lines Outside LTE, 1988, pp. 273–275. doi:10.1007/978-94-009-4023-9_32.
[50] G.B. Scharmer, M. Carlsson, A new approach to multi-level non-LTE radiative transfer problems, J. Comput. Phys. 59 (1985) 56–80.
[51] A. Botnen, M. Carlsson, Multi 3D, 3D non-LTE radiative transfer, in: Numerical Astrophysics, Springer, Dordrecht, 1999, pp. 379–382.
[52] I. Hubeny, A computer program for calculating non-LTE model stellar atmospheres, Comput. Phys. Commun. 52 (1) (1988) 103–132.
[53] E. Avrett, R. Loeser, Solar and Stellar Atmospheric Modeling Using the Pandora Computer Program, Proceedings of the International Astronomical Union 210, 2003.
[54] I. Hubeny, O. Blaes, J.H. Krolik, E. Agol, Non-LTE models and theoretical spectra of accretion disks in active galactic nuclei. IV. Effects of compton scattering and metal opacities, Astrophys. J. 559 (2001) 680–702.
[55] D. Darby-Lewis, J. Tennyson, K.D. Lawson, S.N. Yurchenko, M.F. Stamp, A. Shaw, S. Brezinsek, Synthetic spectra of BeH, BeD and BeT for emission modeling in JET plasmas, J. Phys. B At. Mol. Opt. Phys. 51 (18) (2018) 185701.
[56] A.M. Amarsi, M. Asplund, The solar silicon abundance based on 3D non-LTE calculations, Mon. Not. R. Astron. Soc. 464 (2017) 264–273.
[57] T.A.A. Sigut, Non-LTE Calculations for the C II Doublet System, Astrophys. J. 473 (1) (1996) 452–463.
[58] K. Lind, M. Asplund, P.S. Barklem, A.K. Belyaev, Non-LTE calculations for neutral Na in late-type stars using improved atomic data, Astron. Astrophys. 528 (2011) 1–9.
[59] K. Wada, R. Fukushige, T. Izumi, K. Tomisaka, Circumnuclear Multi-phase Gas in the Circinus Galaxy. I. Non-LTE Calculations of CO Lines, Astrophys. J. 852 (2018) 88.
[60] A.M. Amarsi, M. Asplund, R. Collet, J. Leenaarts, The Galactic chemical evolution of oxygen inferred from 3D non-LTE spectral-line-formation calculations, Mon. Not. R. Astron. Soc. Lett. 454 (2015) L11–L15.
[61] P.S. Barklem, A.K. Belyaev, A. Spielfiedel, M. Guitou, N. Feautrier, Inelastic Mg +H collision data for non-LTE applications in stellar atmospheres, Astron. Astrophys. 541 (2012) A80.
[62] P.S. Barklem, A.K. Belyaev, A.S. Dickinson, F.X. Gadéa, Inelastic Na+H collision data for non-LTE applications in stellar atmospheres, Astron. Astrophys. 519 (2010) A20.
[63] C.E. Treanor, J.W. Rich, R.G. Rehm, Vibrational relaxation of anharmonic oscillators with exchange-dominated collisions, J. Chem. Phys. 48 (1968) 1807–1813.
[64] A. Pastorek, S. Civiš, V.H.J. Clark, S.N. Yurchenko, M. Ferus, Time-resolved Fourier transform infrared emission spectroscopy of CO v = 1 and v = 2 extended bands in the ground $X^1\Sigma^+$ state produced by formamide glow discharge, J. Quant. Spectrosc. Radiat. Transf. 262 (2021) 107521.
[65] K. Kawaguchi, Y. Hama, S. Nishida, Time-resolved Fourier transform infrared spectroscopy: application to pulsed discharges, J. Mol. Spectrosc. 232 (2005) 1–13.
[66] S. Civiš, P. Kubát, S. Nishida, K. Kawaguchi, Time-resolved Fourier transform infrared emission spectroscopy of H_3^+ molecular ion, Chem. Phys. Lett. 418 (2006) 448–453.
[67] S.N. Yurchenko, A.F. Al-Refaie, J. Tennyson, EXOCROSS: a general program for generating spectra from molecular line lists, Astron. Astrophys. 614 (2018) A131.
[68] E. Pannier, C.O. Laux, RADIS: A nonequilibrium line-by-line radiative code for CO_2 and HITRAN-like database species, J. Quant. Spectrosc. Radiat. Transf. 222–223 (2019) 12–25.
[69] Y.B. Band, K.F. Freed, Dissociation processes of polyatomic molecules, J. Chem. Phys. 63 (1975) 3382–3397.
[70] M.J. Berry, Golden rule calculation of reaction product vibronic state distributions, Chem. Phys. Lett. 27 (1) (1974) 73–77.
[71] V.S. Nguyen et al., Theoretical Study of Formamide Decomposition Pathways, J. Phys. Chem. A 115 (2011) 841–851.
[72] G. Panelli et al., Investigating resonant low-energy electron attachment to formamide: Dynamics of model peptide bond dissociation and other fragmentation channels, Phys. Rev. Res. 3 (2021) 013082.
[73] A. Gahlaut, M. Paranjothy, Unimolecular decomposition of formamide: Via direct chemical dynamics simulations, Phys. Chem. Chem. Phys. 20 (2018) 8498–8505.
[74] H.T. Nguyen, V.S. Nguyen, N.T. Trung, R.W.A. Havenith, M.T. Nguyen, Decomposition pathways of the neutral and protonated formamide in some lower-lying excited states, J. Phys. Chem. A 117 (2013) 7904–7917.
[75] D. Liu, W.H. Fang, X.Y. Fu, Ab initio molecular orbital study of the mechanism of photodissociation of formamide, Chem. Phys. Lett. 318 (2000) 291–297.
[76] J. Tennyson et al., The 2020 release of the ExoMol database: Molecular line lists for exoplanet and other hot atmospheres, J. Quant. Spectrosc. Radiat. Transf. 255 (2020).
[77] C.M. Western et al., The spectrum of N_2 from 4,500 to 15,700 cm^{-1} revisited with PGOPHER, J. Quant. Spectrosc. Radiat. Transf. 219 (2018) 127–141.
[78] J.S.A. Brooke et al., Line strengths of rovibrational and rotational transitions in the $X^2\Pi$ ground state of OH, J. Quant. Spectrosc. Radiat. Transf. 168 (2016) 142–157.
[79] G. Li, I.E. Gordon, L.S. Rothman, Y. Tan, S.-M. Hu, S. Kassi, A. Campargue, E.S. Medvedev, Rovibrational line lists for nine isotopologues of the CO molecule in the $X^1\Sigma^+$ ground electronic state, Astrophys. Journal 216 (1) (2015) 15.
[80] P.F. Bernath, MoLLIST: molecular line lists, intensities and spectra, J. Quant. Spectrosc. Radiat. Transf. 240 (2020).
[81] Y. Wang, J. Tennyson, S. Yurchenko, Empirical line lists in the ExoMol database, Atoms 8 (1) (2020) 7.
[82] G.J. Harris, J. Tennyson, B.M. Kaminsky, Y.V. Pavlenko, H.R.A. Jones, Improved HCN/HNC linelist, model atmospheres and synthetic spectra for WZ Cas, Mon. Not. R. Astron. Soc. 367 (2006) 400–406.
[83] R.J. Barber et al., ExoMol line lists – III. An improved hot rotation-vibration line list for HCN and HNC, Mon. Not. R. Astron. Soc. 437 (2013) 1828–1835.
[84] S.N. Yurchenko, T.M. Mellor, R.S. Freedman, J. Tennyson, ExoMol line lists-XXXIX. Ro-vibrational molecular line list for CO_2, Mon. Not. R. Astron. Soc. 496 (2020) 5282–5291.
[85] S.N. Yurchenko, T.M. Mellor, Treating linear molecules in calculations of rotation-vibration spectra, J. Chem. Phys. 153 (15) (2020) 154106.
[86] NIST Diatomic Spectral Database. <www.physics.nist.gov/PhysRefData/MolSpec/Diatomic/index.html>.
[87] K.P. Huber G.H. Herzberg Molecular Spectra and Molecular Structure IV Constants of Diatomic Molecules, Springer, 1979.
[88] A.M. Syme, L.K. McKemmish, Experimental energy levels of $^{12}C^{14}N$ through MARVEL analysis, Mon. Not. R. Astron. Soc. 499 (2020) 25–39.
[89] A.A. Kutepov, L. Rezac, A.G. Feofilov, Evidence of a significant rotational non-LTE effect in the CO_2 4.3 μm PFS-MEX limb spectra, Atmos. Meas. Tech. 10 (2017) 265–271.
[90] G. Gilli et al., Limb observations of CO_2 and CO non-LTE emissions in the Venus atmosphere by VIRTIS/venus express, J. Geophys. Res. E Planets 114 (2009) 1–19.